Research Article

SOHAG JOURNAL OF SCIENCES

https://doi.org/10.21608/sjsci.2022.153658.1017

Influence of Fe Substitution on Structural Morphological and Magnetic Properties of $Zn_{1-x}Fe_xO$ Thin Films to Various Applications

A. Z. Mahmoud[1,2], E. M. M. Ibrahim[3], Lamiaa Galal[1,3,4,*], and E. R. Shaaban[5]

[1] *Physics Department, Faculty of Science, Assiut University, Assiut 71516, Egypt.*
[2] *Physics Department, College of Sciences and Art At ArRass, Qassim University, ArRass 51921, Kingdom of Saudi Arabia.*
[3] *Physics Department, Faculty of Science, Sohag University, Sohag 82524, Egypt.*
[4] *Physics Department, Faculty of Science, Northern Border University, Arar 91431, Kingdom of Saudi Arabia.*
[5] *Physics Department, Faculty of Science, Al-Azhar University, Assiut 71542, Egypt.*
[*] *Email: lamiaa.galal2@nbu.edu.sa*

Received: 1st August 2022, **Revised:** 8th September 2022, **Accepted:** 9th September 2022.
Published online: 1st January 2023

Abstract: The crystalline structure characteristics, morphological (through SEM), and magnetic properties of $Zn_{1-x}Fe_xO$ thin films produced by the sol-gel spin coating process on glass substrates were examined to gain a better understanding of the effects of Fe in ZnO (x=0.0, 0.05, 0.10, 0.15, and 0.20). X-ray diffraction (XRD) and energy dispersive analysis X-ray techniques are used to explore the impact of Fe doping on the structural ZnO nanocrystalline films (EDAX). In order to investigate the XRD patterns of $Zn_{1-x}Fe_xO$, The XRD data demonstrated that Fe ions successfully replaced the Zn^{2+} lattice positions after Zn^{2+} replacement without causing any appreciable structural change, and their crystallinity decreased with increasing Fe doping level. Additionally, the XRD investigation supported the hexagonal wurtzite structure's purity. Calculations have been made for the lattice constants, cell volume, atomic packing fraction, and surface density. $Zn_{1-x}Fe_xO$ thin films' microstructural characteristics, crystallite size, and lattice strain were computed. The changes in microstructural parameters were discussed in detail as a function of Fe concentration. The Zn–O bond lengths and bond angle of $Zn_{1-x}Fe_xO$ were determined and have changed. Magnetization measurements using a vibrating sample magnetometer revealed hysteresis loops in Fe-doped ZnO films and confirmed ferromagnetism at room temperature.
Keywords: Fe doped ZnO, Structure parameters, Bond length, Bond angle, SEM, magnetic properties.

1. Introduction

Indium oxide (In_2O_3), tin oxide (SnO_2), and zinc oxide (ZnO), whether pure or doped, have all been the subject of extensive research recently for optoelectronic and spintronic devices. ZnO has emerged as a leading metal oxide among all of these. It is readily available, non-toxic, and reasonably priced when compared to other materials. A binary semiconductor is ZnO. (II-VI). [1-8]. The direct band gap of ZnO, an n-type metal oxide semiconductor, fluctuates between 3.44 eV at low temperatures and 3.37 eV at room temperature, with a significant exciton binding free energy (60 MeV) at room temperature [9]. The crystal structure of ZnO is wurtzite hexagonal [10]. The electrical conductivity of ZnO is inherently defective due to its wide band gap, such as interstitial zinc atoms and oxygen vacancies [11]. So far, many different methods have been developed to fabricate ZnO nanopowders and thin film studies [12]. In addition, various methods such as sol-gel [13], co-precipitation method [14], sputtering [15] chemical bath deposition [16], hydrothermal [17], spray pyrolysis [18], thermal evaporation [19] and microwave synthesis [20] were used. It has many applications such as cathode ray tubes, light emitting diodes, laser diodes, transparent electrodes for solar cells, surface acoustic wave (SAW) devices, hydrogen storage, ceramics, catalysts, antibacterial activity, photoelectric switches, selective filters in gas sensors [21], transparent thin film transistors, UV detectors, and antifungal agents [22]. ZnO's electrical and optical characteristics can be changed by adding impurities using the right procedure [23]. Doping ZnO with iron is intended to change ZnO's absorbance and other physical or chemical characteristics [24]. Impurities have a significant impact on the physical characteristics of ZnO, including electrical conductivity, piezoelectricity, and defect structure [25]. Several dopants such as Fe, Cr, Al, Cu, Co, Mn, Mg, S, P, etc. can lead to increased surface area of ZnO-based powders. Fe^{3+}doped ZnO nanoparticles with lower crystallinity and high surface area have been reported to have higher catalytic activity and higher sensitivity than pure ZnO or Fe_2O_3 [26]. The prospect of integrating intrinsic magnetic and electronic functionality into a single material has spurred intense interest in developing thin wide-bandgap semiconductor magnetometer systems with room-temperature RT ferromagnetism [27]. In our study, we used a low-cost sol-gel spin coating process to deposit $Zn_{1-x}Fe_xO$ thin films on a glass substrate with fixed thicknesses (200 nm) of x=0.0, 0.05, 0.10, 0.15, and 0.20. Scanning Electron Microscopy (SEM) was used to examine the morphology of the films, and a number of structural parameters, including the lattice constant, cell volume, atomic packing fraction, and surface density, were computed.

$Zn_{1-x}Fe_xO$ thin films' microstructural characteristics, crystallite size, and lattice strain were computed. The analysis indicates that the $Zn_{1-x}Fe_xO$ thin films were uniformly distributed with smooth grain boundaries. It is possible to have a thorough grasp of the numerous physical qualities that depend on surface morphology and structural features for diverse applications by comparing these parameters of all ZnO films with varied Fe contents. Studies of the magnetic characteristics of thin $Zn_{1-x}Fe_xO$ films have also been described. It is possible to interpret the change in magnetic characteristics in terms of microstructural parameters.

2. Experimental

Thin film prepared by sol-gel spin coating technique. Zinc acetate dehydrate ($Zn(CH_3COO)_2.2H_2O$), isopropanol (C_3H_7OH) and monoethanolamine (C_2H_7NO) were used as precursor, solvent, and solution stabilizer, respectively. Ferric acetate hydrate ($(CH_3COO)_2Fe.H_2O$ is also used as a doping element. A 0.5 M ZnO solution was prepared by dissolving 1.0975 g of zinc acetate in 10 ml of isopropanol and then adding different amounts of different concentrations of the doping element (iron acetate) to the solution. The doping concentration of Fe in the ZnO solution was kept at 0%, 5%, 10%, 15% and 20%. Stir the solution vigorously for 60 min at 65 ^oC using a magnetic stirrer on a hot plate. Maintaining a 1:1 molar ratio of zinc acetate to monoethanolamine, the cloudy solution became homogeneous and transparent by adding monoethanolamine dropwise to the solution. The solution was stirred for a further 1 hour and aged at room temperature for 24 hours. Glass microscope slides pre-cleaned with an ultrasonic cleaner were used to develop doped ZnO thin films by sol-gel technique. The deposition of the film was performed by a conventional spin coater rotated at 2000 rpm .The prepared samples were placed on a hot plate at150 ^oC for 10 min for preheat treatment. Film thickness was raised to 200 nm by repeating the process of spin coating and preheat treatment 8 times. The films were finally annealed at 500 $^oC$for 2 h in a conventional muffle furnace.

The structure and the phases of $Zn_{1-x}Fe_xO$ thin films films were investigated by X-ray diffraction pattern (XRD Philips 1710). In addition, the configurational characteristics and elemental analysis of Zn, O and Fe are determined by the energy dispersion of the X-ray (EDAX) interfaced with a scanning electron microscope, SEM (JEOL JSM-6360LA, Japan) operating an accelerating voltage of 30 kV. The virtual error of the indicated elements unexceeds 2%. Using the vibrating sample magnetometer model (VSM-9600M-1, USA), studied the magnetic properties of the prepared films. The measurements were conducted in a maximum applied field of 15 kOe at temperature equal to RT.

3. Results and discussion

3.1. Energy-dispersive analysis X-ray (EDAX) spectra

In order to explore the elemental makeup of the produced samples and validate the successful doping and production of ZnO NPs, energy dispersive X-ray investigations (EDAX) were carried out. The spectra in Fig. 1 provide an energy dispersive X-ray study of Fe-doped ZnO semiconductor films (a and b). The lack of contaminants in the spectrum is another intriguing observation. Additional evidence of sample purity. The sample treated with 10% Fe showed iron peaks along with zinc and oxygen.

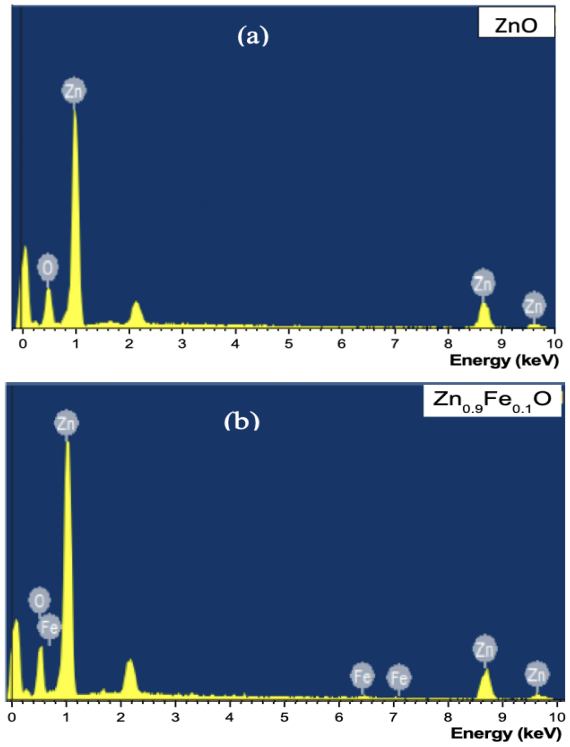

Fig. 1: Energy-dispersive analysis X-ray (EDAX) spectrum of (a) ZnO, (b) $Zn_{0.9}Fe_{0.1}O$ thin films

3.2. XRD analysis

Fig. 2 displays the X-ray diffraction patterns of pure ZnO and Fe-doped ZnO thin films. The hexagonal wurtzite phase formed in a polycrystalline phase, according to the XRD patterns of the ZnO samples. The ZnO (100), (002), (101), (102), (110), (103), and (112) planes are where the diffraction peaks are directed. According to JCPDS data card #01-079-0208, all peaks are consistent. ZnO was found to have a preferential c-axis orientation along the (002) plane, which made crystal development easier due to low internal stress, low surface free energy, and high atomic density. Even so, the peak positions for various Fe:ZnO dopant concentrations vary slightly, suggesting that iron binds to ZnO without altering the crystal structure [28,29]. The full-width at half-maximum (FWHM) corresponding to these planes increases with the increase of Fe-doping concentrations (0, 5, 10, 15 and 20 at. %, respectively).

The intensities of the (100), (002) and (101) peaks gradually decrease with increasing Fe doping concentration, as shown in Fig. 2. The decay of the peak indicated that the substitution of Fe^{3+} ions by Zn^{2+} ions inhibited the crystal growth of ZnO. This is related to the Fe doping concentration that affects the stress of ZnO films [30]. The shift of the peak position to higher angles is evident, and the distance between

the planes becomes shorter due to the strain within the ZnO lattice. From the above results, it can be concluded that an appropriate Fe doping concentration will reduce the crystal quality of ZnO, and it is also confirmed that ZnO and Fe doped ZnO are the most stable phases [31]. The peak shifts correspond to the elongation of the compounds and the substitution of Fe for some of the zinc cations in each compound. Replacing iron in the lattice with zinc changes the elongation, as shown by the peak shift [32]. It is observed that an increase in the concentration of Fe by more than 15 % led to forming another phase named spinel (Fe_2O_3).

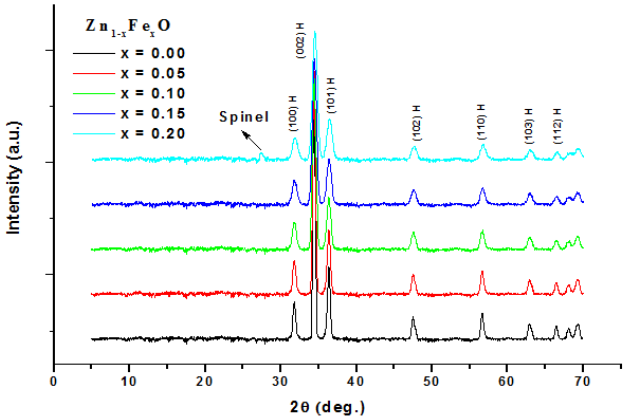

Fig. 2. XRD patterns of $Zn_{1-x}Fe_xO$ films with different Fe composition (x=0, 0.05, 0.10, 0.15 and 0.20 mol).

3.3. The lattice parameters

The lattice parameters 'a' and 'c' of the wurtzite structure of ZnO and Fe-doped ZnO films can be calculated using the plane spacing equation [33].

$$\frac{1}{d_{hk\ell}^2} = \frac{4}{3}\left(\frac{h^2 + hk + k^2}{a^2}\right) + \frac{\ell^2}{c^2} \qquad (1)$$

Where a & c are the lattice parameters, d is the interplanar distance and (hkl) are the Miller indices with the first-order approximation (n = 1) for the (100) plane and using the Bragg equation $n\lambda = 2d_{hk\ell}sin\theta$ The lattice parameter 'a' and 'c' is obtained from the relations

$$a = \frac{\lambda}{(\sqrt{3}\sin\theta_{100})} \quad \& \quad c = \frac{\lambda}{\sin\theta_{002}} \qquad (2)$$

The values of lattice parameters "a" and "c" are in good agreement with the standard values for ZnO single crystals (a = 3.250 Å and c = 5.207 Å), indicating the quality of the ZnO thin films. The values of lattice parameters "a" and "c" are lower than those of bulk doped films, which are strong indicators of compressive stress in the films [34]. In Fig. 3, it can be observed that the lattice parameters "a" and "c" decrease with increasing iron content in $Zn_{1-x}Fe_xO$. The lattice parameter c/a ratio is almost equal to 1.6 which indicates that the shape of ZnO and Fe doped ZnO wurtzite structures is reasonably perfect. The values of c/a listed in Table 1.

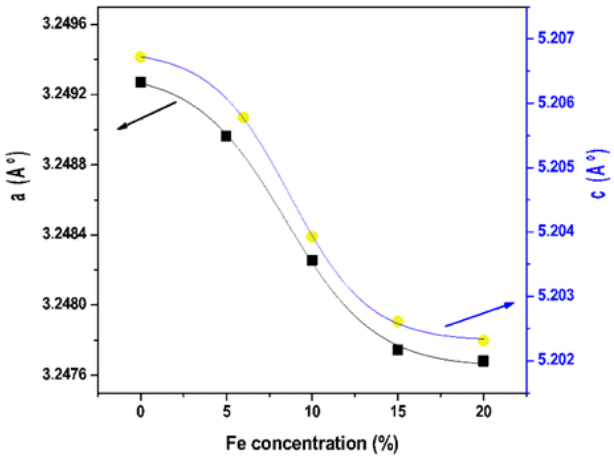

Fig. 3. Lattice parameters "a" and "c" against Fe concentration for $Zn_{1-x}Fe_xO$ thin films.

3.4. Atomic Packing Fraction (APF)

It defines as the fraction of volume in a crystal structure that is occupied by constituent particles. It is a dimensionless quantity and always less than unity. Atomic packing fraction (APF) for hexagonal was calculated by using the formula [35]. Where a and c are lattice parameters [36]. The results show that the APF increases with the iron content, which may be due to the increase of voids in the samples. The APF of the bulk hexagonal ZnO material is about 75%, but in this study, the APF of the $Zn_{1-x}Fe_xO$ film is greater than 75%, indicating that the APF in the nanocrystals is slightly larger than that in the bulk material. This is attributed to size effects in nanocrystalline thin films. The APF increases with the Fe content in the $Zn_{1-x}Fe_xO$ films, indicating uniform substitution of Fe ions in the zinc sites of the ZnO structure [37]. The atomic packing fractions (APFs) of the Zn_{1-x} Fe_xO films are listed in Table 2.

Table 1: Morphological parameters of $Zn_{1-x}Fe_xO$ thin films

Conc. X (%)	c/a	V (Å)^3	ε_a	ε_c
0	1.60243	47.60652	0.07722	0.05811
5	1.60229	47.58885	0.07712	0.05792
10	1.60207	47.55144	0.07689	0.05754
15	1.60192	47.52416	0.07671	0.05728
20	1.60185	47.51966	0.07669	0.05722

3.5. Volume of unit cell and X-ray density

The volume of unit cell was calculated using the equation [38]

$$V = \frac{\sqrt{3}}{2}a^2c \qquad (6)$$

where a & c are lattice parameters. It is found that the unit cell volume decreases with increasing iron content, which can be attributed to the decrease of the unit cell volume values shown in Table 1. This suggests that iron ions have moved to available zinc sites in the structure.

The number of unit cells in the particle is calculated from the equation [39].

$$N = \frac{4}{3\pi\frac{D}{2V}} \quad (7)$$

The X-ray density of ZnO sample was calculated by using the formula [40].

$$\rho = \frac{nM}{N_A V} \quad (8)$$

Where, ρ is X-ray density, n is the number of atoms per unit cell, M is the molecular weight of the sample N_A is Avogadro's number and V is the volume of unit cell. The X-ray density higher with increasing Fe content of $Zn_{1-x}Fe_xO$ nanoparticles. This may be due to a decrease in unit cell volume and a decrease in sample molecular weight. The molecular weight of Fe ions (55.845 amu) is smaller than that of Zn ions (65.38 amu). As the Fe content increases, the volume of the unit cell decreases and the X-ray density increases. This means that Fe ions enter the Zn sites in the ZnO structure [41].

3.6. Specific surface area

It is a property of solids defined as the total surface area of a material per unit of mass and can be used to determine the type and properties of a material. The values obtained for specific area depend on the method of measurement. The specific surface area can be calculated from particle size given by [42].

$$S = \frac{6x\,10^8}{Dx\,\rho} \quad (9)$$

The specific surface area decreases with iron incorporated as shown in Table 2.

Table 2: Dislocation density δ, X-ray density ρ, packing factor P and surface energy S respectively for $Zn_{1-x}Fe_xO$ thin films.

Conc. x %	δ x 10^{-4} $(nm)^{-2}$	ρ (g/cm^3)	P %	S (cm^2/g)
0	18	5.68	75.46	44.76
5	20	5.68	75.467	47.28
10	26	5.68	75.477	53.62
15	45	5.69	75.485	70.76
20	81	5.69	75.487	95.08

3.7. Crystal size and lattice strain

The average crystalite size D of the prepared films has been calculated using a well-known Debye–Scherer's formula [38]

$$D = \frac{k\lambda}{\beta_{Crystallite}\cos\theta} \quad (10)$$

The average particle size of Fe-doped ZnO sample was decreased with increasing in the weight content of Fe dopant due to the distortion of ZnO host lattice caused by the addition of Fe ions which can lead to reduce the nucleation and grain growth rates of Fe doped ZnO nanoparticles. Reduction of average crystallize size indicates merging from good crystallinity. The calculated crystallite size values shown in Fig 4. From this study, dislocation density (δ) and lattice strain of estimated samples are calculated by using following equation:

$$\delta = \frac{1}{D^2} \quad (11)$$

The dislocation density of any material provides the quality of films and its defect structure of the material. The dislocation density usually is defined as the number of dislocations per unit length or per unit area of desired samples. In the present study, incorporation of Fe doping in The ZnO matrix, the dislocation density gradually increases which indicates its defect structure. Strain towards c-axis and towards a- axis can be calculated from the formula $\varepsilon_c = ((c-c_\circ)/c_\circ)\times 100\%$ and $\varepsilon_a = ((a-a_\circ)/a_\circ)\times 100\%$. The δ and "ε_a, ε_c" data are tabulated in Table 2 and 1 respectively.

The lattice strain (ε) can be calculated from Stoke and Wilson Eq. [43].

$$\varepsilon = \frac{\beta_{Strain}}{4tan\theta} \quad (12)$$

Where, K is the shape factor, which is a constant taken as 0.94 λ is the wavelength of the X-ray radiation (λ=1.5416 Å), θ is the Bragg's angle in degree and β is the full width at the half maximum (FWHM) of the prepared films. The β can be corrected form the following relationship

$$\beta = \sqrt{\beta_{obs}^2 - \beta_{std}^2} \quad (13)$$

Where β_{obs} is the integral peak profile width of sample, and β_{std} is the peak profile width of standard (silicon).

Fig. 4 displays the average crystallite size and lattice strain of the pure ZnO and Fe/ZnO films. While the lattice strain rises with increasing Fe inclusion, the crystallite size decreases. Due to the fact that the ionic radius of Fe (Fe^{3+}: 0.645) is somewhat less than the ionic radius of Zn (Zn^{2+}: 0.60) for the same coordination number, both the trend of D and may be attributed to the change in the lattice size with Fe substitution by Zn (four-fold coordination). The observed decrease of D and increases in lattice strain can be attributed to the combined effects of (i) lattice distortion of the host ZnO crystal because of the substitution of smaller ionic-sized iron atoms sitting in the ZnO lattice [44] and (ii) hindering of the crystal growth due to the formation of a thin layer of Fe–O–Zn on the surface of the doped samples due to the presence of excessive iron ions in the precipitation solution [45].

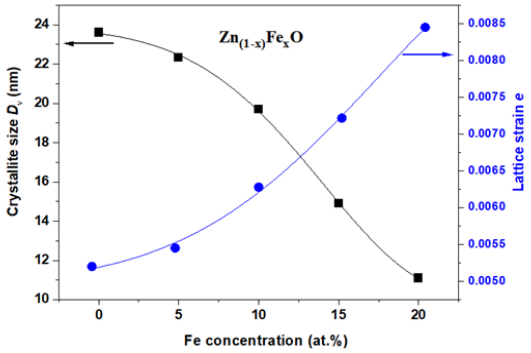

Fig. 4: Crystallite size and lattice strain $Zn_{1-x}Fe_xO$ films as a function of Fe content.

3.8. Bond length and bond angle

Different atoms all combine and form stable compounds. Bonds are formed to achieve this bonding. Ionic or electrovalent bonds, covalent bonds, and coordinate bonds are among the several types of bonding. This in turn shows that each bond is linked to a certain asset. The bond length is the separation between the nuclei of two bound atoms when they are in equilibrium. The bond length decreases as the attraction between the bound atoms increases. However, the bond length increases with increasing atomic size. A complex molecule's or ion's core atom is the subject of two orbitals that contain a pair of bonding electrons, and the angle between them is referred to as the bond angle.

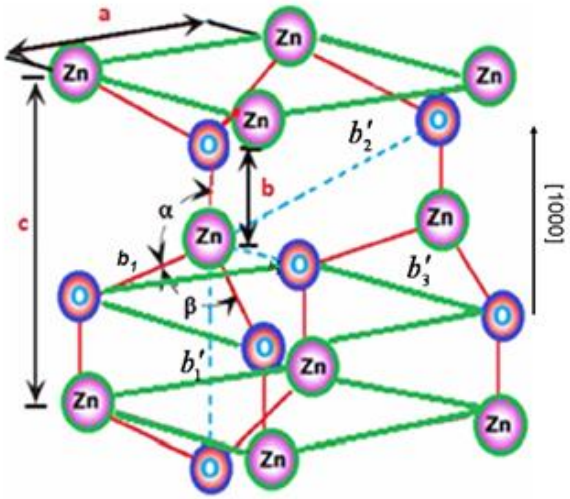

The Zn–O bond length L is given by [46]

$$L = \sqrt{\left(\frac{a^2}{3} + c^2\left(\frac{1}{2} - u\right)^2\right)} \quad (14)$$

where a and c are lattice parametes, *u* is the positional parameter in the wurtzite structure and measures the amount which each atom gets displaced with respect to the next [47]. and *u* is given by

$$u = \frac{a^2}{3c^2} + \frac{1}{4} \quad (15)$$

The Zn–O bond length calculated according to this study is from 1.9758 Å to1.9763Å. whereas the reported Zn–O bond length in the unit cell of ZnO and neighboring atoms is 1.9767 Å [48]. There is a good agreement of the calculated & actual bond length which supports the results of present study. The value of bond length is given in Table 3.

In additional, there are three types of second-nearest neighbors, which designated as b_1' (one along the direction), b_2' (six of them) and b_3' (three of them) with the bond lengths, shown in Fig. 5 are calculated as [49]

$$b_1' = c(1 - u) \quad (16)$$

$$b_2' = \sqrt{a^2 + (uc)^2} \quad (17)$$

$$b_3' = \sqrt{\frac{4a^2}{3} + \left(\frac{1}{2} - u\right)^2 c^2} \quad (18)$$

As the Fe doping concentration increases, the distance of the second-nearest neighbors also decreases. This is due to the increased occupancy of the dopant. The variation of the second-nearest neighbor as a function of Fe doping concentration is Table 3. It is interesting to note that both distances b_2' and b_3' are equal for Wurtzite geometry. The bond angles are given by,

$$\alpha = \frac{\pi}{2} + cos^{-1}\left[1 + 3\left(\frac{c}{a}\right)\left(-u + \frac{1}{2}\right)^2\right]^{-1} \quad (19)$$

$$\beta = 2sin^{-1}\left[\frac{4}{3} + 4\left(\frac{c}{a}\right)^2\left(-u + \frac{1}{2}\right)^2\right]^{-1} \quad (20)$$

The calculated bond angles are coinciding with the standard value ($\alpha = \beta$ = 109.47). The ratio between α and β is one for the ideal case. But the ratio is 0.98 for the Fe doped ZnO nanoparticles irrespective of the Fe doping concentration. All the evaluated values are presented in Table 3.

Table 3: The values of Positional parameter, bond length and bond angle for undoped and Fe doped ZnO.

Conc. x %	u	*b* (Å)	b_1' (Å)	b_2' (Å)	b_3' (Å)	α (°)	β (°)
0	0.3798141	1.977586	3.229134	3.803761	3.803761	108.4474	110.4754
5	0.3798362	1.977344	3.228436	3.803371	3.803371	108.4427	110.4798
10	0.3798726	1.97683	3.2271	3.802506	3.802506	108.4351	110.4871
15	0.3798969	1.976455	3.226155	3.801867	3.801867	108.43	110.492
20	0.3799071	1.976394	3.225916	3.801784	3.801784	108.4279	110.4941

3.9. Scanning Electron Microscopy (SEM)

It has been found from Fig. 6 that the average grain size reduces due to Fe-doping which may support the reduction of intensity along (002) planes. The surface morphology and particle size of pure and doped (Fe) ZnO nanoparticles were analyzed by using SEM. The entire SEM pictures clearly shows the samples consists of mostly spherical shaped and the average size of the nanoparticles is of the order of nanometer size. The SEM images exhibit particle size of Fe-doped ZnO powder which are in the range 33, 28, 24, 19 and 15 nm. Another lucid visualization from the SEM images indicates increasing the Fe-doping percentage causes a gradual decrease in average grain size. The Fe-doped ZnO samples were composed of spherical nanoparticles with agglomeration increasing of particles due to the decrease of surface energy of nanoparticles. In our present study, increasing doping percentages cause a decrease in interstitial Zinc due to the dopant's concentration. Therefore, the grain growth of ZnO was inhibited due to the decreasing of diffusivity.

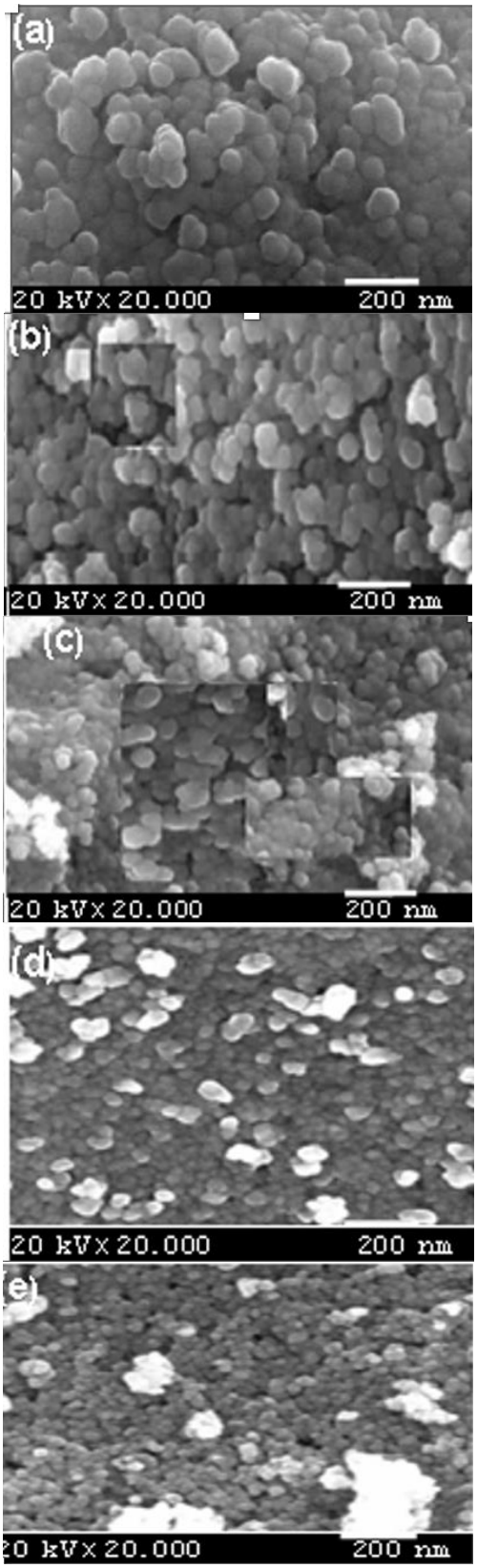

Fig. 6: SEM micrographs of $Zn_{1-x}FexO$ thin films with (x=0, 0.05, 0.10, 0.15 and 0.20 mol.).

3.10. Magnetic characterization

To better understand the magnetic behavior of these Fe-doped ZnO nanoparticles with different concentrations (0%, 5%, 10%, 15% and 20%), magnetization against field-dependent curves were measured at 300 K. Fig. 7 exhibits pure ZnO diamagnetic performance, whereas Fe/ZnO nano-particles reveal RTFM and magnetization rises with increasing Fe content. There was no indication of saturation in every of the considered samples. Based on the XRD and SEM results, a possible clarification for the origin of RTFM in Fe-doped ZnO nanoparticles can be originate. These results indicate that Fe^{3+} ions occupy Zn^{2+} sites within the lattice of the wurtzite ZnO crystal structure.

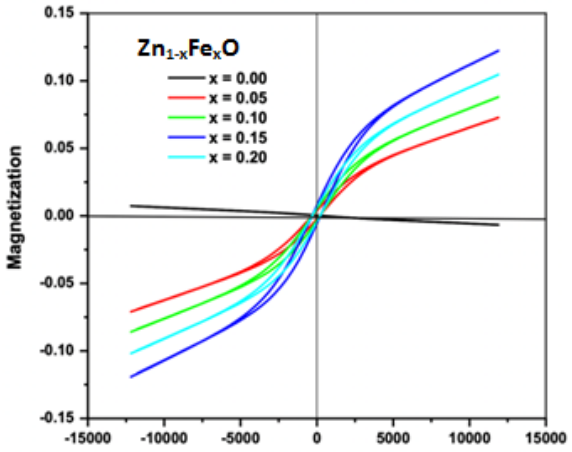

Fig. 7. Room temperature Magnetic hysteresis loops for $Zn_{1-x}Fe_xO$ ($0.0 \leq x \leq 0.20$) thin films.

It can be seen that the M-H plot of all Fe-doped ZnO nanoparticles show the formation of hysteresis loops, which means that the room-temperature ferromagnetic behavior with small coercive field and low remanence exhibits soft ferromagnetism. Several groups have reported that iron-doped ZnO nanoparticles are ferromagnetic at and/or above room temperature [50, 51] . It has been proposed that the change in magnetization in Fe-doped ZnO is due to the shortening of the average distance between Fe ions with increasing Fe content [52, 53]. Therefore, the weak magnetization observed at low Fe levels in this work can be attributed to the larger distance between Fe ions, which weakens the ferromagnetic interaction.

However, by increasing the iron content, the ferromagnetic interaction becomes stronger (shorter iron ion spacing), thereby increasing the magnetization. The magnetic moment of the materials increases with the increasing Fe doping concentration for all the samples except with high concentration 20%. This is attributed to the upgrowth of a binary phase that reduces the magnetism of this concentration. This phase is the spinel that appeared in the XRD spectra. There is no doubt that this phase is (Fe_2O_3) a ferrite material that obstructs the magnetic field and reduces the magnetism of the material as shown in Fig. 7.

4. Conclusions

In order to explore the behaviour of ZnO based thin films as a function of Fe concentration, different compositions of dilute semiconductor $Zn_{1-x}Fe_xO$ thin films were produced onto glass substrates using sol-gel dip-coating process. The XRD results showed that the Fe ions successfully occupied the Zn^{2+} lattice positions without significantly altering the structure that was impacted by the Zn^{2+} substitution. The quality of the ZnO thin films is shown by the computed values of the lattice parameters "a" and "c," which are in good agreement with the standard values for ZnO single crystals (a = 3.250 and c = 5.207). With increased Fe inclusion, the crystallite size shrinks (from 24 to 11 nm), yet the lattice strain grows (from 0.0052 to 0.0085). Both trend of *D* and ε may attribute to that the ionic radius of Fe (Fe^{3+}: 0.69 Å) is slightly smaller the ionic radius of Zn (Zn^{2+}: 0.74 Å) for the same coordination number (four-fold coordination). The second-nearest neighbor distances were calculated for Fe doping ZnO nanoparticles for the first time. Magnetic tests at RT revealed ferromagnetism in all Fe-doped ZnO sheets till 15 %. It is possible to attribute the ferromagnetic behaviour seen in the ZnO lattice to the substitution of Fe ions by Zn ions. These findings indicate that the Fe-doped ZnO film can be recommended for optoelectronic and spintronic device applications

References

[1] A. Dev, S. Chaudhuri, B. Dev, *Bulletin of Materials Science*, 31 (2008) 551-559.

[2] F. A. Mahmoud, G. Kiriakidis, *Journal of Ovonic Research*, 5 (2009) 15-20.

[3] N. Kakati, S. H. Jee, S. H. Kim, J. Y. Oh, Y. S. Yoon, *Thin Solid Films*, 519 (2010) 494-498.

[4] C. Y. Wang, V. Cimalla, T. Kups, C.-C. Röhlig, H. Romanus, V. Lebedev, J. Pezoldt, T. Stauden, O. Ambacher, *Journal of Applied Physics*, 102 (2007) 044310.

[5] A. Murali, A. Barve, V. J. Leppert, S. H. Risbud, I. M. Kennedy, H. W. Lee, *Nano Letters*, 1 (2001) 287-289.

[6] N. Van Hieu, N. A. P. Duc, T. Trung, M. A. Tuan, N. D. Chien, *Sensors and Actuators B: Chemical*, 144 (2010) 450-456.

[7] A. Azam, A. S. Ahmed, M. S. Ansari, A. H. Naqvi, *Journal of alloys and compounds*, 506 (2010) 237-242.

[8] T. N. Soitah, Y. Chunhui, S. Liang, *Science of Advanced Materials*, 2 (2010) 534-538.

[9] M. Ginting, S. Taslima, K. Sebayang, D. Aryanto, T. Sudiro, P. Sebayang, *AIP Conference Proceedings*, 62 (2017) 30-39.

[10] A. Srivastava, R. Gakhar, P. Dua, K. Senthil, J. Tawale, K. Sood, K. Yong, *Microscopy*, 1 (2010) 1820-1823.

[11] A. S. Menon, N. Kalarikkal, S. Thomas, *Studies*, 1 (2013) 41-45.

[12] T. T. Ha, T. D. Canh, N. V. Tuyen, *International Scholarly Research Notices*, 9 (2013) 245-249.

[13] M. Vafaee, M. S. Ghamsari, *Materials Letters*, 61 (2007) 3265-3268.

[14] K. Raja, P. Ramesh, D. Geetha, *Spectrochimica acta part A: molecular and biomolecular spectroscopy*, 131 (2014) 183-188.

[15] C.-f. Fu, X.-m. Chen, L. Li, L.-f. Han, X. Wu, *Optoelectronics Letters*, 6 (2010) 37-40.

[16] C.-H. Ku, J.-J. Wu, *Nanotechnology*, 18 (2007) 505706.

[17] D. Ramimoghadam, M. Z. Hussein, Y. H. Taufiq-Yap, *Chemistry Central Journal*, 7 (2013) 1-10.

[18] T. Ogi, D. Hidayat, F. Iskandar, A. Purwanto, K. Okuyama, *Advanced Powder Technology*, 20 (2009) 203-209.

[19] J. Wu, T. Li, C. Wang, B. Zhu, R. Wu, C. Xie, *Ceramics International*, 37 (2011) 3469-3476.

[20] T. Prakash, R. Jayaprakash, G. Neri, S. Kumar, *Journal of Nanoparticles*, 8 (2013) 75-79.

[21] S. Sriram, K. Lalithambika, A. Thayumanavan, *Optik*, 139 (2017) 299-308.

[22] Y. Kumar, A. K. Rana, P. Bhojane, M. Pusty, V. Bagwe, S. Sen, P. M. Shirage, *Materials Research Express*, 2 (2015) 105017.

[23] Z. N. Kayani, A. Afzal, F. Saleemi, S. Riaz, S. Naseem, *IEEE Transactions on Magnetics*, 50 (2014) 1-4.

[24] R. Rahimi, J. Shokrayian, M. Rabbani, *The 17th International Electronic Conference on Synthetic Organic Chemistry*, 7 (2013) 95-107.

[25] X. Wang, Z. Wu, J. Webb, Z. Liu, *Applied Physics A*, 77 (2003) 561-565.

[26] L. Fang, X. Zu, Z. Li, S. Zhu, C. Liu, W. Zhou, L. Wang, *Journal of alloys and compounds*, 454 (2008) 261-267.

[27] T. Herng, S. P. Lau, S. F. Yu, H. Yang, L. Wang, M. Tanemura, J. Chen, *Applied physics letters*, 90 (2007) 032509.

[28] S. Chandrasekaran, *Solar Energy Materials and Solar Cells*, 109 (2013) 220-226.

[29] S. Zahirullah, J. Joseph, P. Fermi, *Materials technology*, 32 (2017) 755-763.

[30] V. Gandhi, R. Ganesan, H. H. Abdulrahman, M. Thaiyan, *The Journal of Physical Chemistry C*, 118 (2014) 9715-9725.

[31] Z. Sayed, J. Joseph, P. Fermi, *Materials technology*, 32 (2017) 755-763.

[32] P. Šutta, Q. Jackuliak, *Materials Structure*, 5 (1998) 52-59.

[33] A. Wilson, *International Union of Crystallography*, 5 (1955) 74-79.

[34] R. Jenkins, *CRC Press*, 5 (1995) 85-97.

[35] S. Thakur, N. Sharma, A. Varkia, J. Kumar, *Advances in Applied Science Research*, 5 (2014) 18-24.

[36] A. Stokes, A. Wilson, *Proceedings of the Physical Society (1926-1948)*, 56 (1944) 174-178.

[37] S. Ilican, Y. Caglar, M. Caglar, *Journal of optoelectronics and advanced materials*, 10 (2008) 2578-2583.

[38] V. Mote, J. Dargad, B. Dole, *Nanosci. Nanoeng*, 1 (2013) 116-122.

[39] P. D. File, *ASTM, Philadelphia, Pa*, 4 (1967) 9-185.

[40] D. Pathinettam, A. Marikani, *Crystal Research and Technology: Journal of Experimental and Industrial Crystallography*, 37 (2002) 1241-1248.
[41] V. Bilgin, S. Kose, F. Atay, I. Akyuz, *Materials Chemistry and Physics*, 94 (2005) 103-108.
[42] D. Muthukrishnan, V. Subramaniam, T. Mahalingam, S. Helen, P. Sumathi, *Int. J. Tourism Res.*, 2 (2017) 51-64.
[43] C. Suryanarayana, M. Norton, *New York*, 4 (2013) 85-89.
[44] C. Muiva, T. Sathiaraj, K. Maabong, *Ceramics International*, 37 (2011) 555-560.
[45] J. Wojnarowicz, R. Mukhovskyi, E. Pietrzykowska, S. Kusnieruk, J. Mizeracki, W. Lojkowski, *Beilstein Journal of Nanotechnology*, 7 (2016) 721-732.
[46] L. Xu, X. Li, Y. Chen, F. Xu, *Applied Surface Science*, 257 (2011) 4031-4037.
[47] O. F. Farhat, M. M. Halim, M. J. Abdullah, M. K. Ali, N. K. Allam, *Beilstein journal of nanotechnology*, 6 (2015) 720-725.
[48] C. Kittel, P. McEuen, P. McEuen, *Wiley New York*, 8 (1996) 42-57.
[49] U. Seetawan, S. Jugsujinda, T. Seetawan, A. Ratchasin, C. Euvananont, C. Junin, C. Thanachayanont, P. Chainaronk, *Mater Sci Appl*, 2 (2011) 1302-1314.
[50] R. Chauhan, A. Kumar, R. Chaudhary, *Asian Journal of Chemistry*, 23 (2011) 41-43.
[51] T. Kataoka, M. Kobayashi, Y. Sakamoto, G. Song, A. Fujimori, F.-H. Chang, H.-J. Lin, D. Huang, C. Chen, T. Ohkochi, *Journal of Applied Physics*, 107 (2010) 033718.
[52] L. Guo, D. Peng, H. Makino, K. Inaba, H. Ko, K. Sumiyama, T. Yao, *Journal of magnetism and magnetic materials*, 213 (2000) 321-325.
[53] J. Coey, A. Douvalis, C. Fitzgerald, M. Venkatesan, *Applied Physics Letters*, 84 (2004) 1332-1334.